Supporting Information

A 3D Four-Fold Interpenetrated Conductive Metal-Organic Framework for Fast and Robust Sodium-Ion Storage

Zhaoli Liu, Juan Chu, Linqi Cheng, Junhao Wang, Chongyi Zhang, Cheng Zhang, Fengchao Cui, Heng-Guo Wang,* and Guangshan Zhu*

Key Laboratory of Polyoxometalate and Reticular Material Chemistry of Ministry of Education and Faculty of Chemistry, Northeast Normal University, Changchun, 130024, P. R. China.

*Corresponding authors.

E-mail: cuifc705@nenu.edu.cn; wanghg061@nenu.edu.cn

Table of Contents

Section S1. Experimental section

1.1 Materials

Anhydrous ethanol, acetone, isopropanol, and *N, N*-dimethylformamide (DMF) were purchased from Innochem. $Cu(OAc)_2$, disodium terephthalate (NaTP) and 2,3,6,7,10,11-hexahydroxytriphenylene (HHTP) were purchased from Energy Chemical. Dibenzo-[g,p]chrysene-2,3,6,7,10,11,14,15-octaol (8OH-DBC) were purchased from Jilin Chinese Academy of Sciences-Yanshen Technology Co., Ltd. All reagents were obtained from commercial sources and used without further purification.

1.2 Synthesis of samples

Cu-DBC was synthesized according to the literature by a solvothermal method.[1] A schlenk tube was charged with $Cu(OAc)_2$ (9 mg), dibenzo-[g,p]chrysene-2,3,6,7,10,11,14,15-octaol (12.9 mg), 750 μL DMF and 3 mL deionized water. After approximately 20 min of ultrasonic treatment, the tube was subjected to three freeze-pump-thaw cycles, evacuated to vacuum and sealed. Then, the tube was placed in an oven with a temperature of 85 °C for 72 h. A dark blue precipitate was isolated by filtration, followed by washing with deionized water and acetone several times and dried overnight in a vacuum at room temperature.

Cu-HHTP was synthesized according to the literature by solvothermal method.[2] A vial was charged with $Cu(OAc)_2$ (17.8 mg), 2,3,6,7,10,11-hexahydroxytriphenylene (19.5 mg), 2 mL isopropanol and 2 mL deionized water. After approximately 20 min of ultrasonic treatment, the vail was placed in an oven with a temperature of 85 °C for 15 h. A dark product was obtained by filtration and washing with water, ethanol, and acetone. Finally, the product was dried overnight in a vacuum at 60 °C.

1.3 Material characterizations

TEM images were performed by JEM-2100F. SEM images were performed by HITACHI SU8010. Powder X-ray diffraction (XRD) measurements were tested on Smartlab (Cu Kα-radiation, λ=0.15405 nm, 40 kV, 30 mA). FT-IR spectra were determined by TJ270-30A. UV-

vis spectra were measured by Shimadzu UV-2550 spectrophotometer within 300-800nm wavelength range. TGA curves were carried out on DSC 200 F3 between 25 and 800 °C at 12 °C min^{-1} under air and N_2 atmosphere. The N_2 adsorption-desorption isotherms were determined at 77 K by using a Quantachrome Autosorb iQ apparatus. The electrodes were analyzed by X-ray photoelectron spectroscopy (XPS, Thermon ESCALAB 250) while all binding energies had to be corrected with C 1s.

1.4 Assembly of batteries and electrochemical measurements

The Cu-DBC or Cu-HHTP cathodes were prepared by casting the slurry, which is composed of Cu-DBC or Cu-HHTP, acetylene black, and sodium carboxymethyl cellulose (CMC) in weight ratio of 6:3:1 or 8:1:1 with deionized water, onto aluminum foil. The disodium terephthalate (NaTP) anode was prepared by casting the slurry, which is composed of NaTP, acetylene black, and polyvinylidene fluoride (PVDF) in a weight ratio of 6:3:1 with N-methyl-2-pyrrolidone (NMP), onto copper foil. The above electrodes were dried at 80 °C in an oven for 12 h. Cu-DBC or Cu-HHTP cathodes load the active material of more than 0.5 mg cm^{-2}.

The electrochemical tests of half-cells and full-cells were performed using 2025 coin-type cells assembled in an Ar-filled glove box. The cathode (or anode) of half cells were assembled containing Cu-DBC/Cu-HHTP (or NaPT) electrodes, 1M $NaPF_6$ in DME as the electrolyte (100 μL), Na metal as the counter electrode and glass fiber (Whatman GF-A) as the separator. The full cell was fabricated using a similar method with that used for the cathode of half cells, except that the pre-sodiated NaTP anode was used instead of Na metal.

Cyclic voltammetry (CVs) measurements were tested by CHI600E electrochemical workstation with the voltage range of 1.0-3.5 V. Electrochemical measurements were performed using the NEWARE battery system with the voltage range of 1.0-3.5 V. Electrochemical impedance spectroscopy (EIS) tests were conducted over a frequency range of 100 kHz-0.1 Hz. The chemical diffusion coefficient of Na^+ ions was tested by galvanostatic intermittent titration technique (GITT) at a current density of 0.05 A g^{-1} for 10 min followed by

30 min of relaxation. $D_S = \frac{4}{\pi\tau}\left(\frac{n_m V_m}{S}\right)^2 \left(\frac{\Delta E_S}{\Delta E_t}\right)^2$, τ is a relaxation time; n_m is the number of moles, and the V_m is the molar volume of the electrode material, and S is an electrode contact area, and ΔE_s is a voltage change caused by pulses, ΔE_t is the voltage change of constant current charge and discharge.

Section S2. Calculation Section

2.1 Calculations of charge storage kinetics

Kinetics can be analyzed using the equation below:

$$i = av^b \quad (1)$$

where i is the peak current and v is the scan rate based on the CV curves.

The capacitive contribution can be calculated by the following equation:

$$i = k_1 v + k_2 v^{1/2} \quad (2)$$

where i, $k_1 v$, and $k_2 v^{1/2}$ represent current, capacitive, and ionic diffusion contributions, respectively.

2.2 DFT computational methods

The quantum chemical calculation of the electronic structure of Cu-DBC fragments was performed by Gaussian 16 package[3] under B3LYP[4, 5]/def2-TZVP[6] level. Electronic structure analyses were conducted using Multiwfn[7] and VMD[8] software.

First-principles calculations for simplified Cu-DBC unit cells have been implemented in the Vienna Ab initio Simulation Package (VASP)[9, 10]. Projector augmented wave (PAW)[11] method was employed to describe core-valence interaction with plane wave cut-off energy of 500 eV. The generalized gradient approximation with the Perdew-Burke-Ernzerhof functional (GGA-PBE)[12] was used to describe the exchange-correlation potential of the electrons. Spin polarization calculations was performed for all simulations with the consideration of empirical dispersions of Grimme (DFT-D3)[13] for the long-range vdW interactions. For an accurate description of the localized d electrons of Cu, the on-site Coulomb interaction was added to the

d orbital of Cu with a U value of 4.0 eV using the rotationally invariant approach of Liechtenstein et al.[14, 15] The Brillouin zone integration was performed by using the k-point sampling of the Monkhorst-Pack scheme with a 2×2×9 grid.[16] The convergence criterion of energy and structural relaxation were set as less than 1.0×10^{-6} eV and 0.02 eV $Å^{-1}$, respectively.

Section S3. Results and Discussion

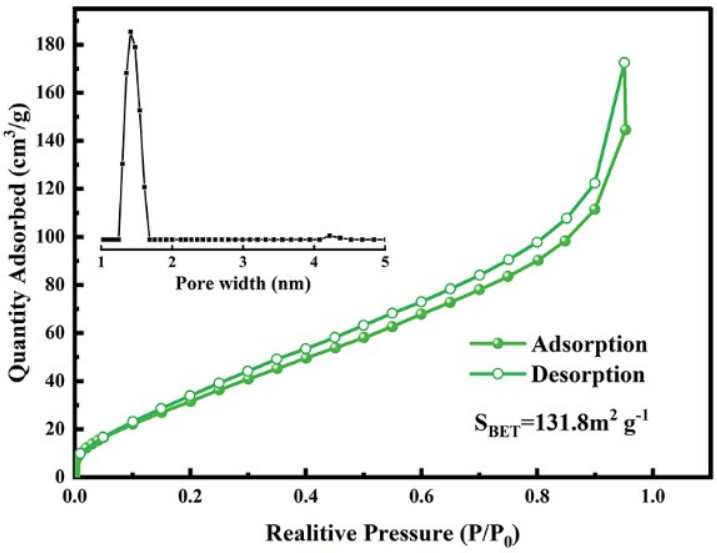

Figure S1. N_2 adsorption-desorption isotherms and pore distribution of Cu-DBC.

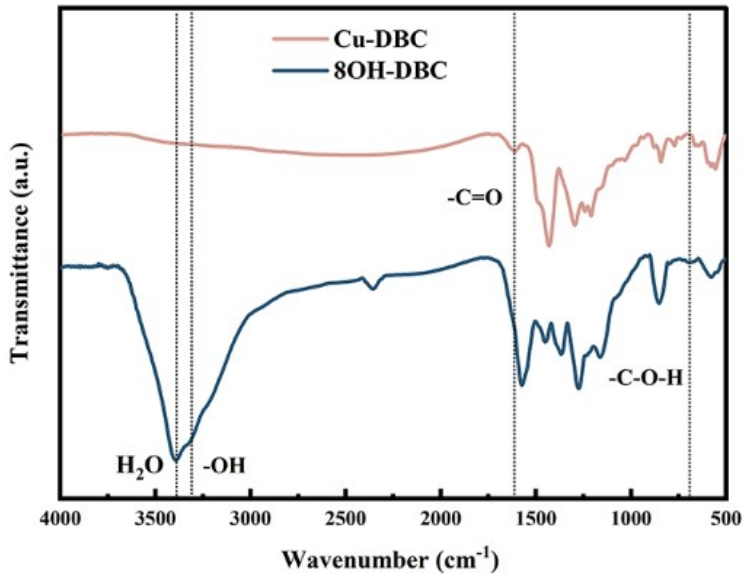

Figure S2. FT-IR spectra of Cu-DBC and 8OH-DBC.

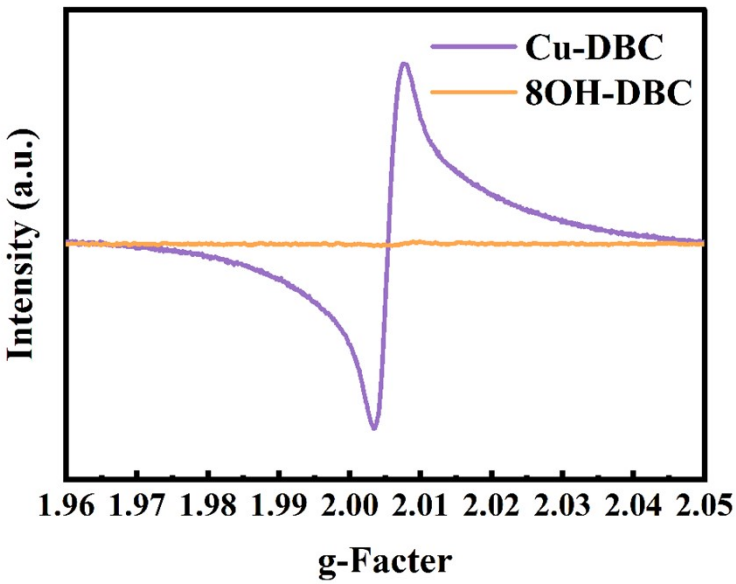

Figure S3. EPR spectra of 8OH-DBC and Cu-DBC.

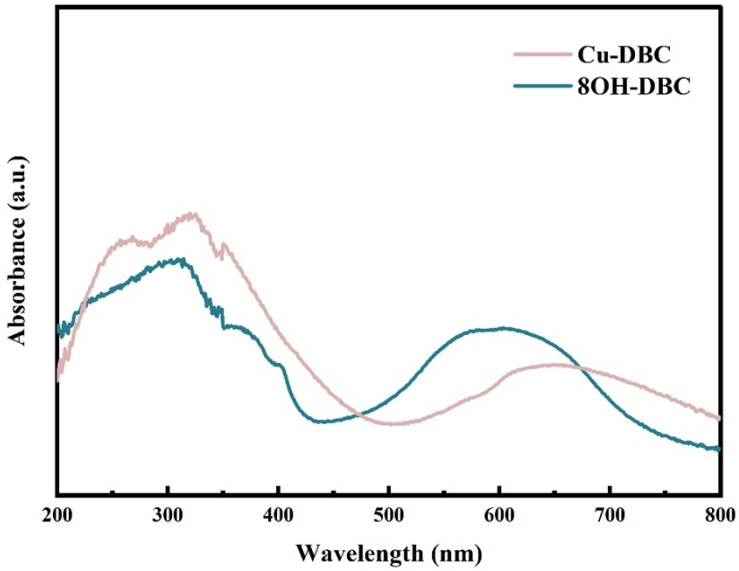

Figure S4. UV-vis spectra of Cu-DBC and 8OH-DBC.

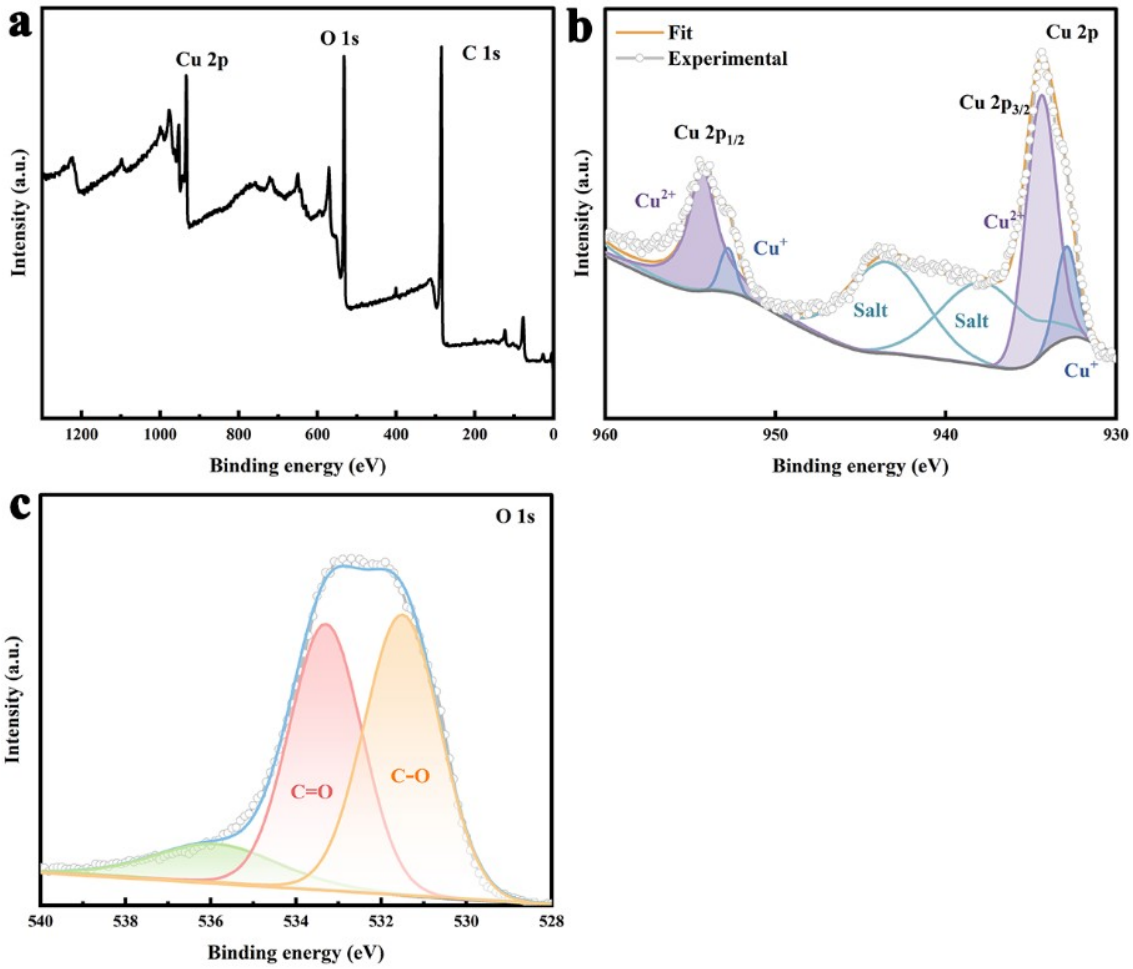

Figure S5. (a) The XPS survey spectrum of Cu-DBC and XPS spectra of (b) Cu 2p and (c) O 1s.

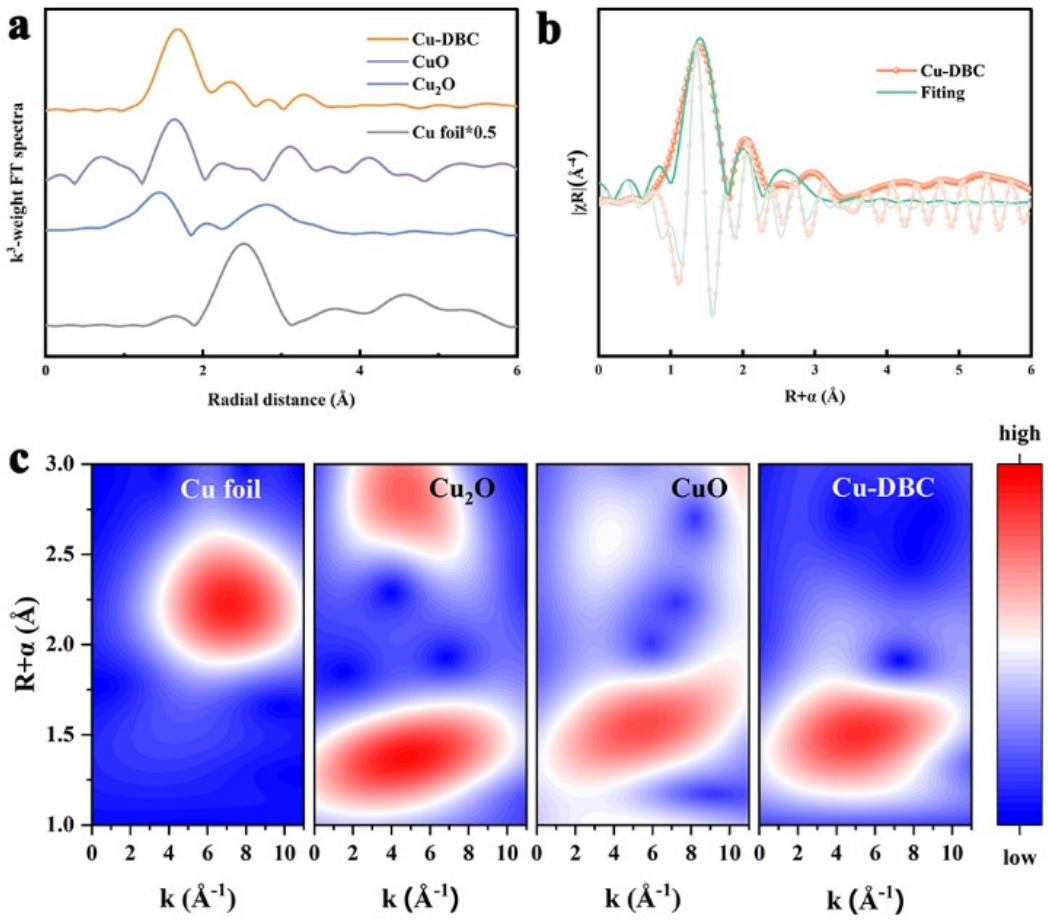

Figure S6. (a) k^3-weighted FT spectra for Cu-DBC, CuO, Cu_2O and Cu foil. (b) k^3-weighted FT-EXAFS experimental and fitting curves of Cu-DBC. (c) Wavelet transform for Cu-DBC, CuO, Cu_2O and Cu foil.

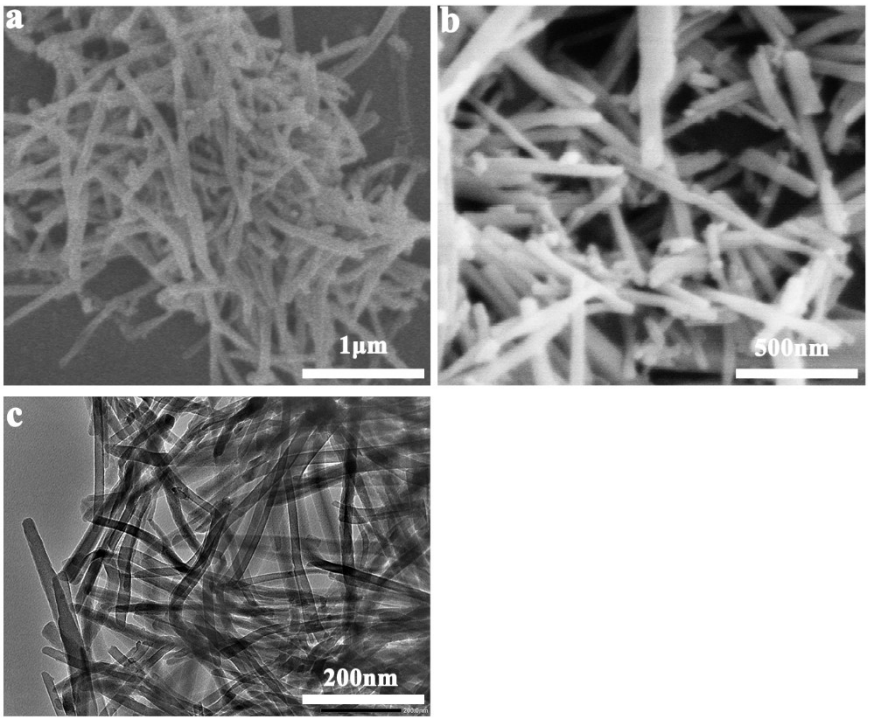

Figure S7. SEM (a-b) and HRTEM (c) images of Cu-DBC.

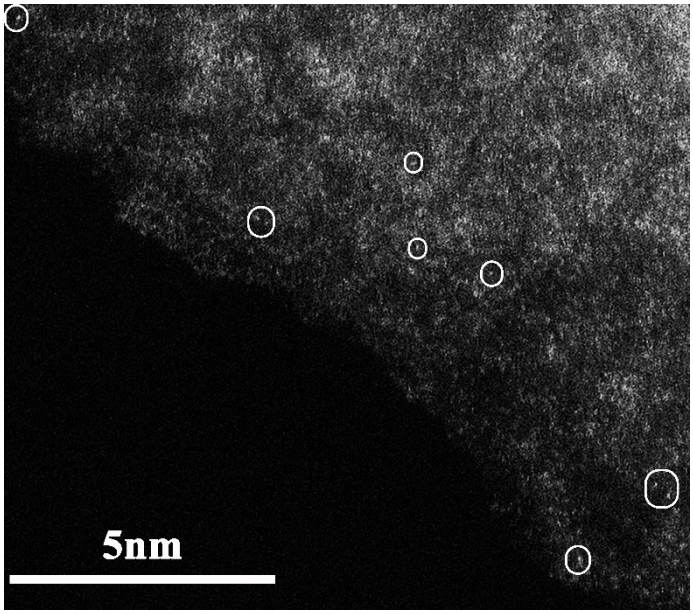

Figure S8. HAADF-STEM image of Cu-DBC.

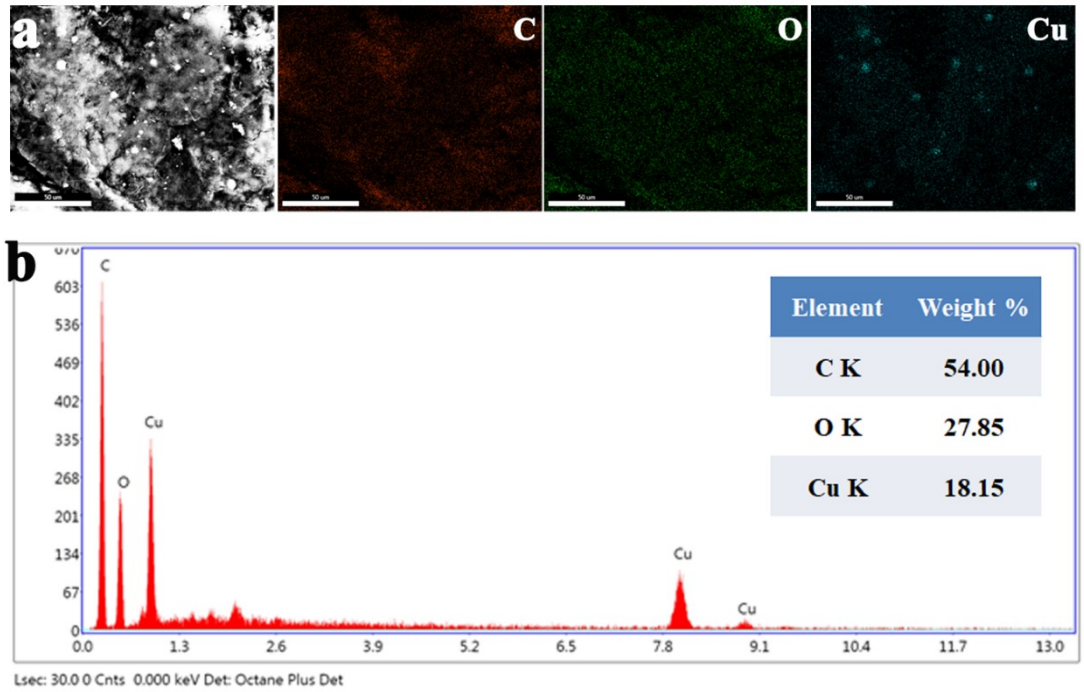

Figure S9. (a) SEM image of Cu-DBC and corresponding element mapping images of C, O, and Cu. (b) The corresponding energy dispersive X-ray spectra of Cu-DBC.

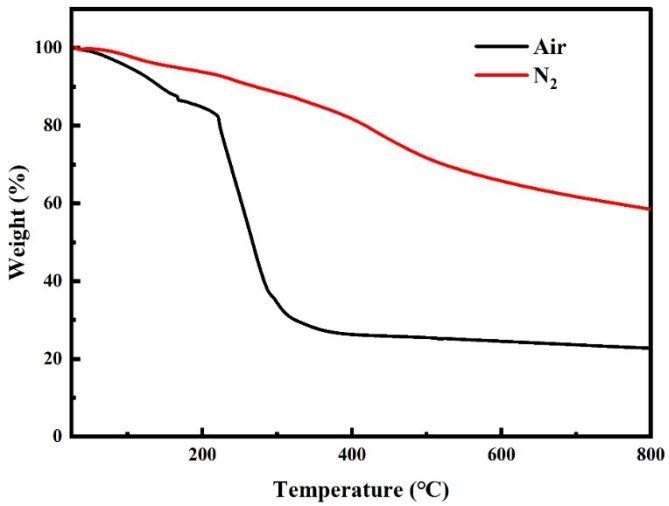

Figure S10. TGA curves of Cu-DBC under Air and N_2 atmosphere.

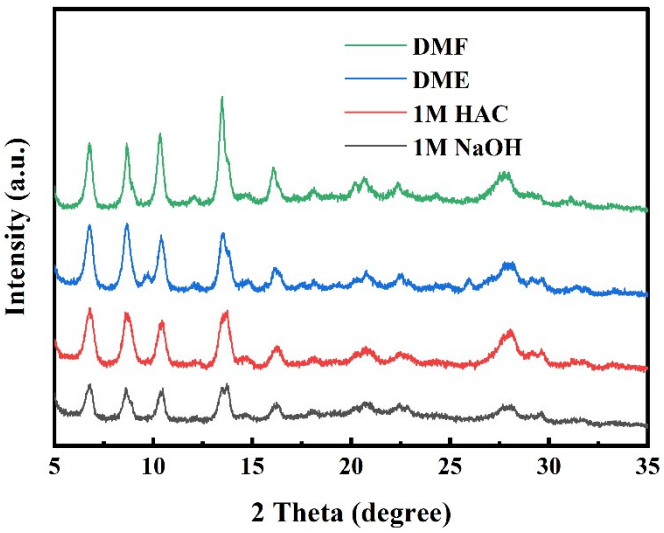

Figure S11. PXRD patterns of Cu-DBC after soaking in organic solvents (DMF), electrolytes (DME), NaOH (1 M) and HAC (1 M).

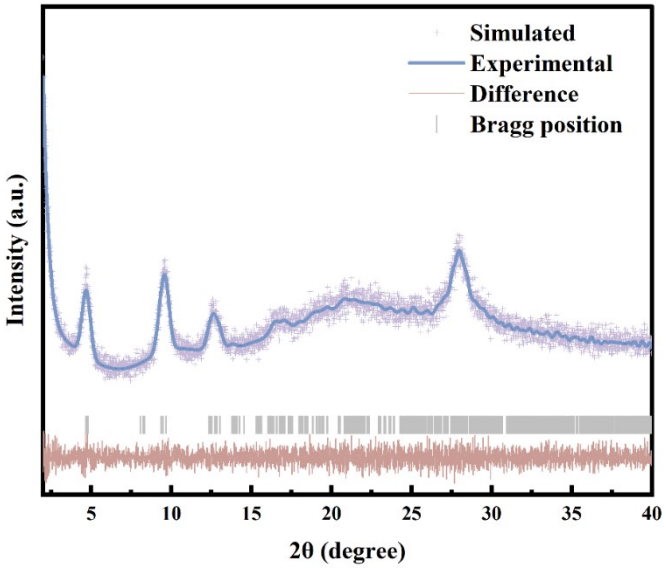

Figure S12. PXRD patterns of Cu-HHTP.

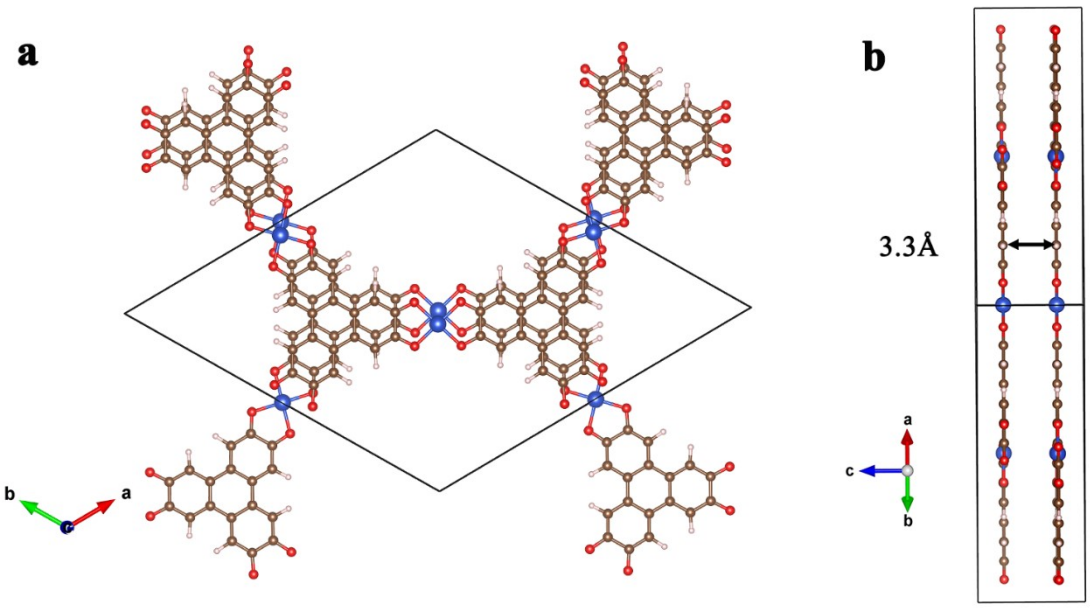

Figure S13. Top view (a) and side view (b) of Cu-HHTP unit cell.

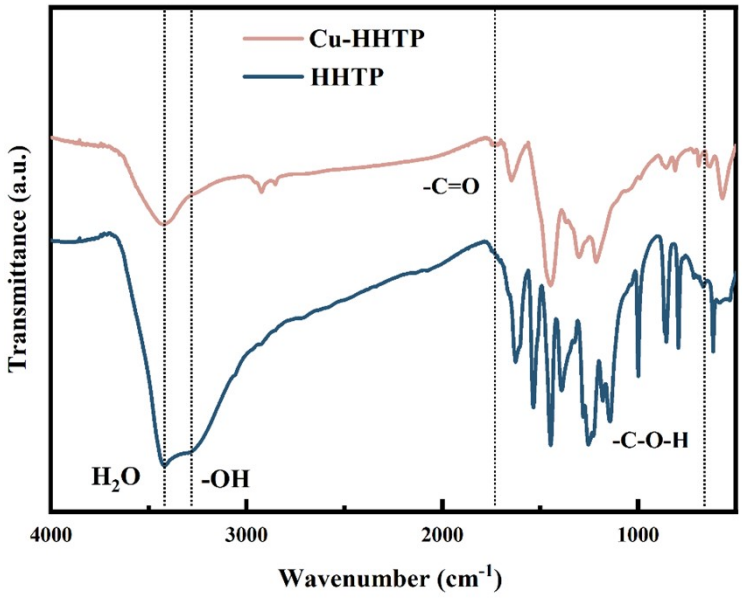

Figure S14. FT-IR spectra of Cu-HHTP and HHTP.

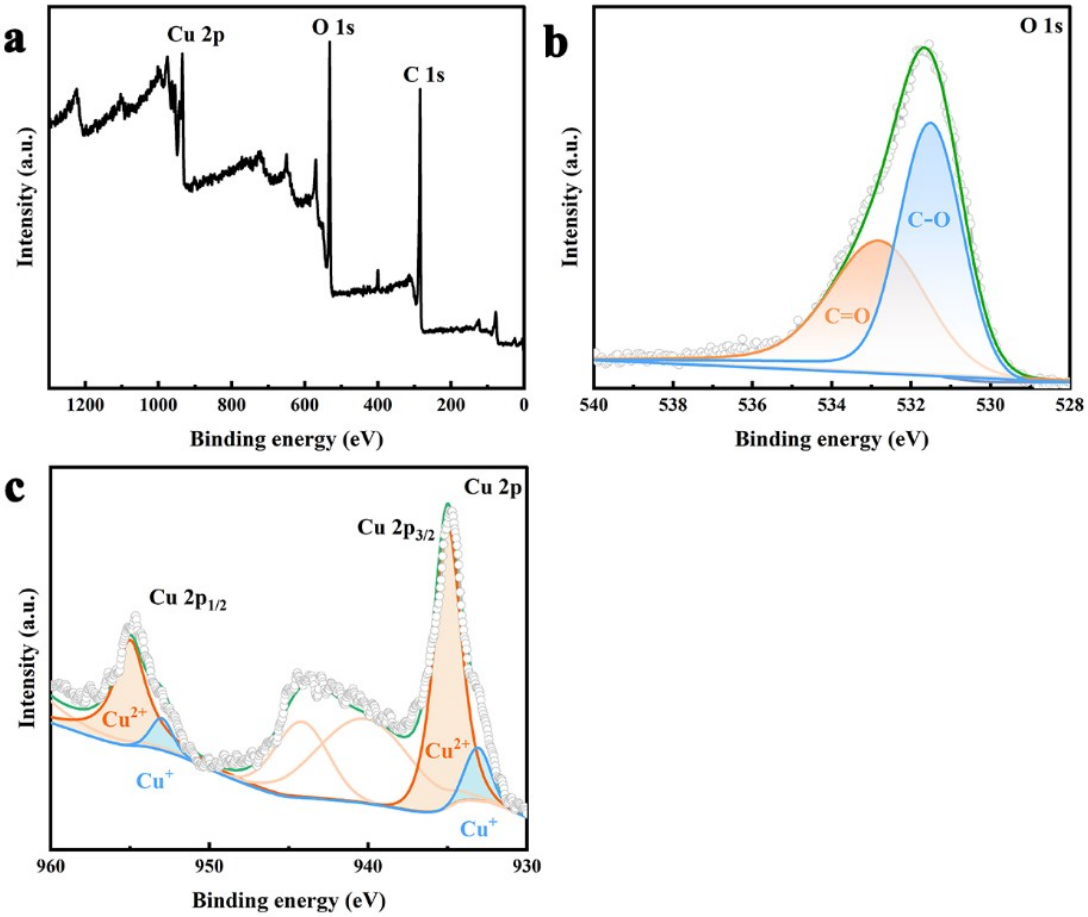

Figure S15. (a) The XPS survey spectrum of Cu-HHTP and XPS spectra of (b) O1s and (c) Cu 2p.

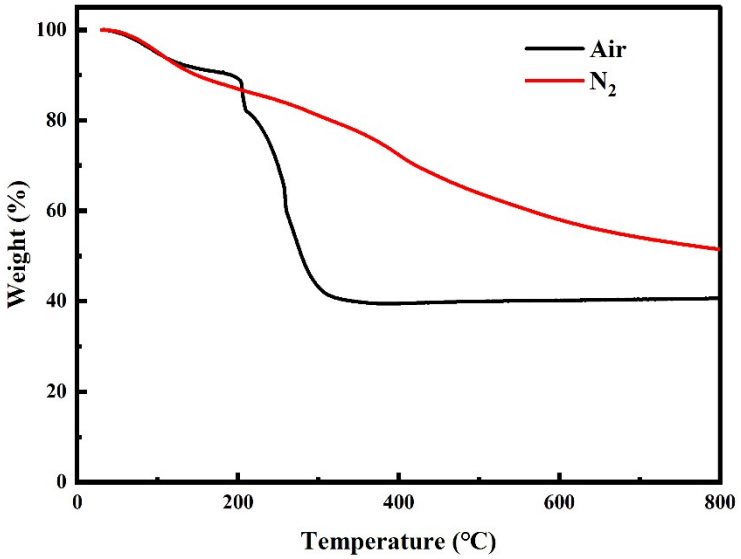

Figure S16. TGA curves of Cu-HHTP at Air and N_2 atmosphere.

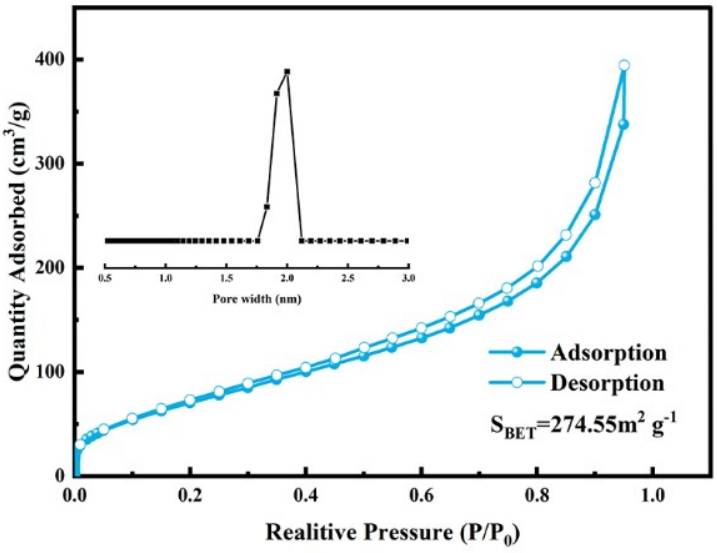

Figure S17. N_2 adsorption-desorption isotherms and pore distribution of Cu-HHTP.

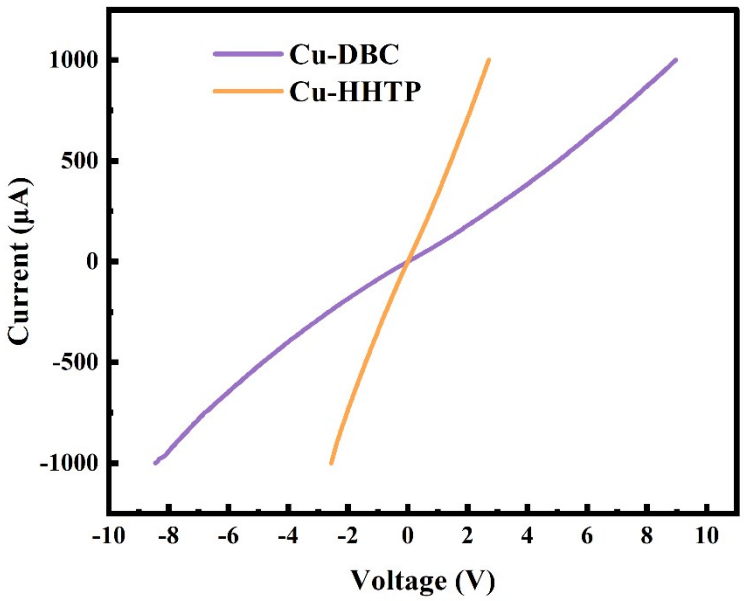

Figure S18. Current-voltage characteristic of Cu-DBC and Cu-HHTP using the two probe method.

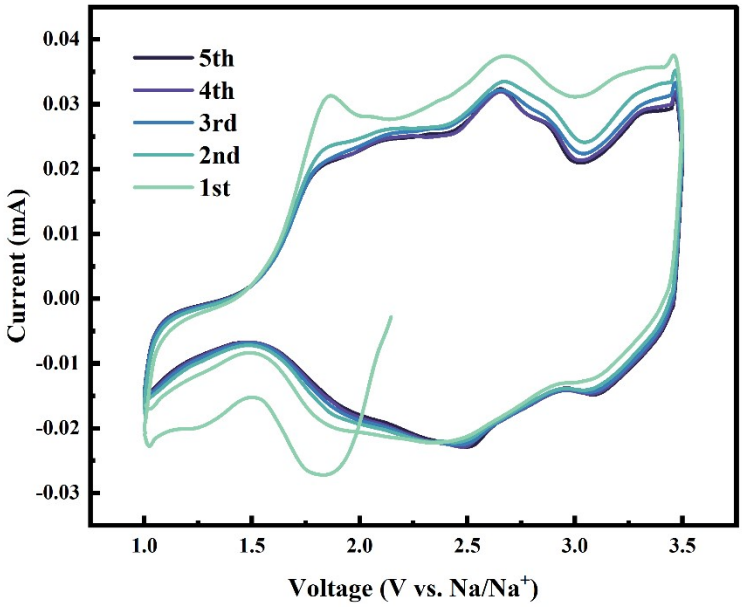

Figure S19. CV curves of Cu-HHTP at 0.1 mV s^{-1}.

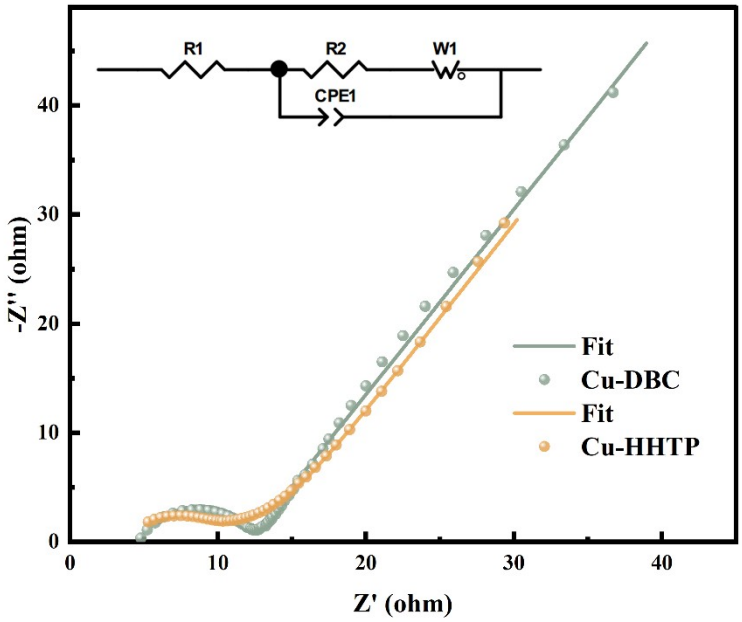

Figure S20. Electrochemical impedance spectra of pristine Cu-DBC and Cu-HHTP.

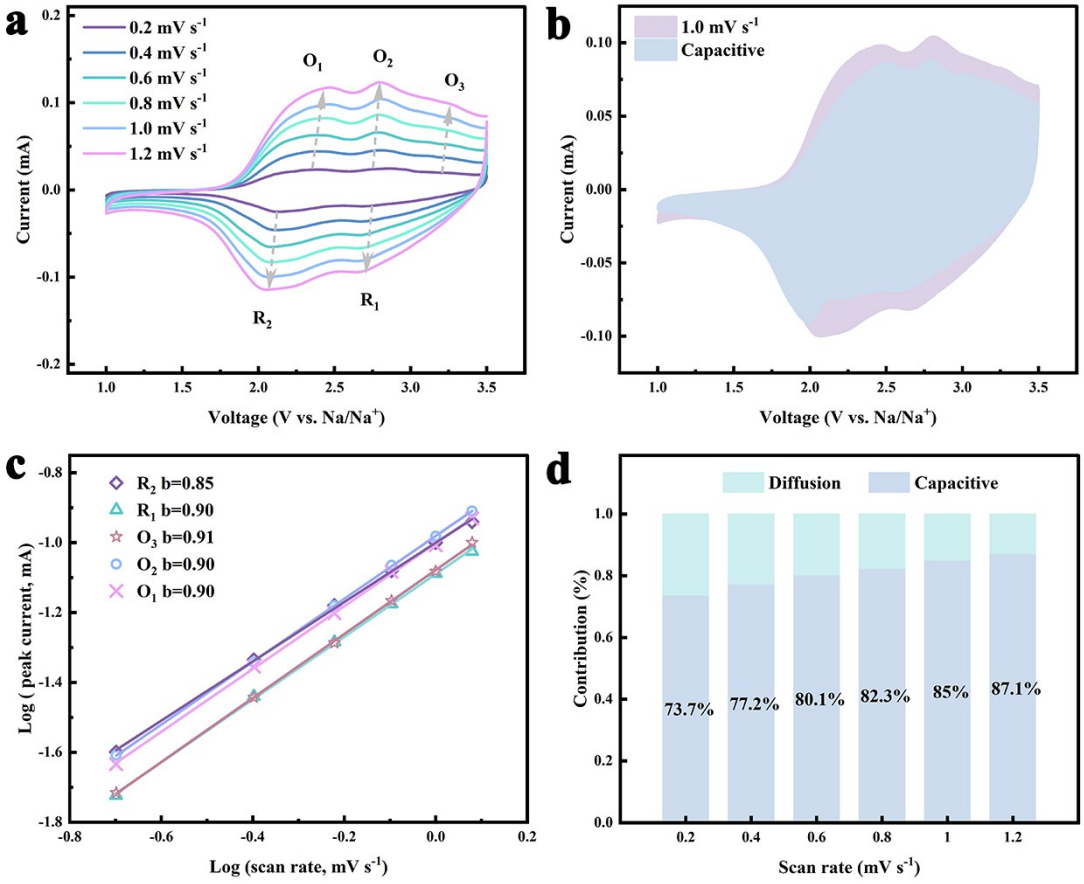

Figure S21. (a) CV curves of Cu-DBC recorded at different scan rates. (b) Capacitive and diffusion-controlled contribution at 1.0 mV s^{-1}. (c) b-value calculated by fitting the plots of log(i) versus log(v). (d) The contribution ratio of the capacitive capacities and diffusion-controlled capacities at different scan rates.

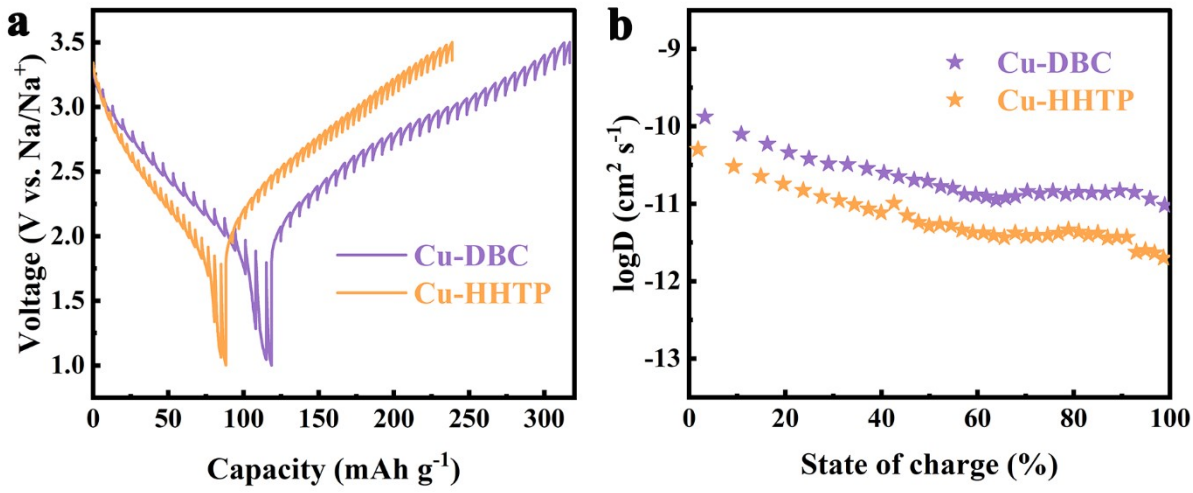

Figure S22. (a) GITT curves of Cu-DBC and Cu-HHTP. (b) LogD (D = Na^+ diffusion coefficient calculated by GITT) of Cu-DBC and Cu-HHTP at the charging state.

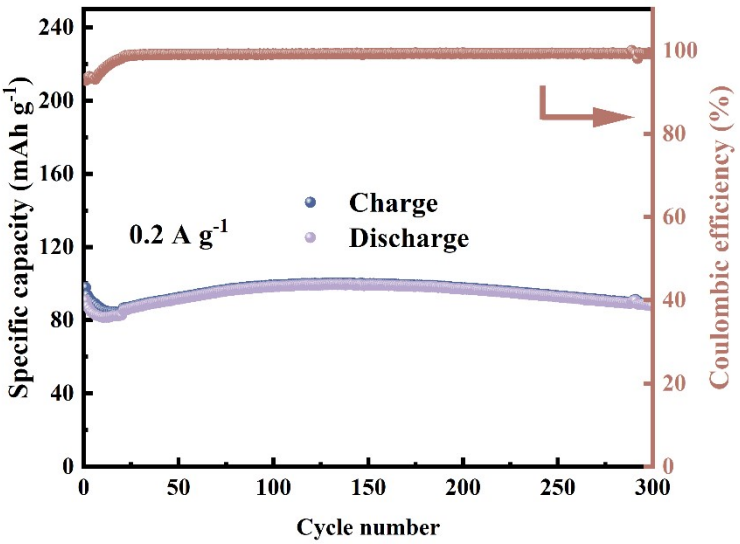

Figure S23. Cycle stability of Cu-DBC with mass-loading of 2.5 mg cm^{-2} at 0.2 A g^{-1}.

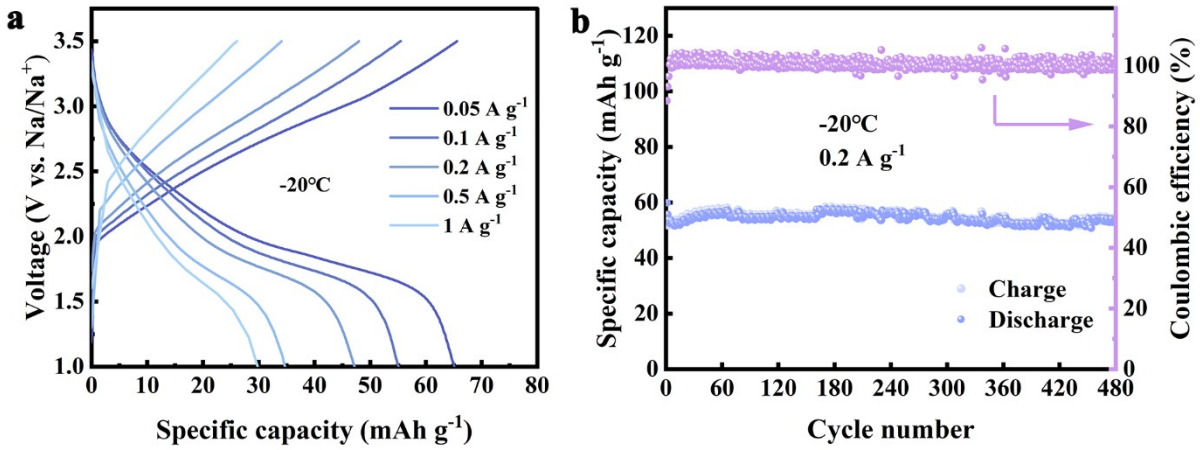

Figure S24. (a) Galvanostatic charge/discharge profiles of Cu-DBC at -20 ℃. (b) Cycle stability of Cu-DBC at -20 ℃.

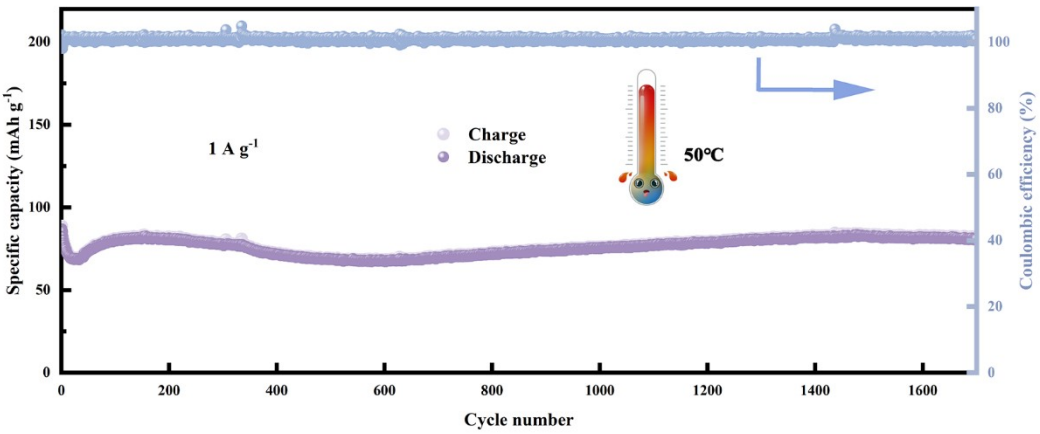

Figure S25. cycle stability of Cu-DBC at 50 ℃.

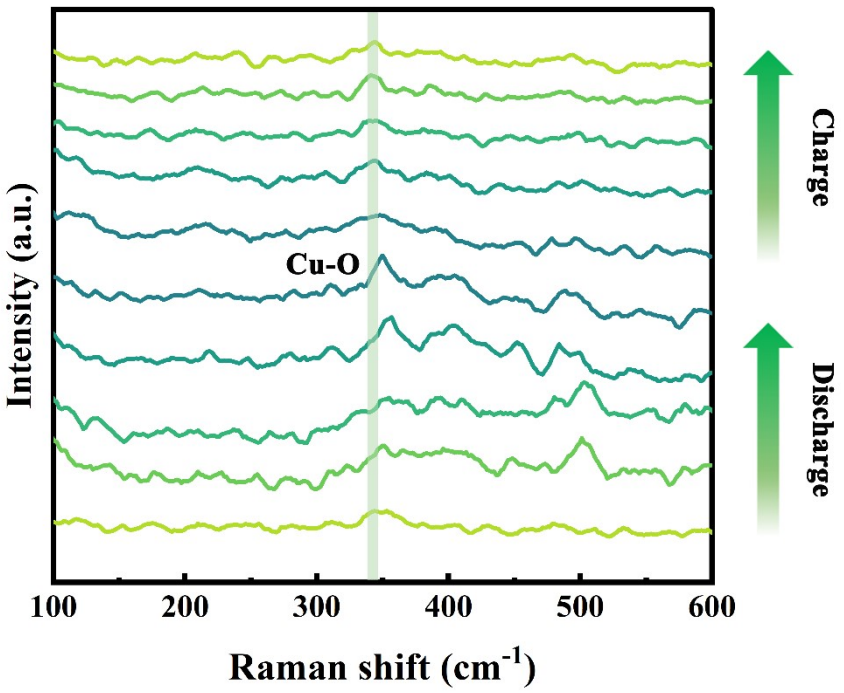

Figure S26. *In situ* Raman spectra of Cu-DBC during the GCD process (the peaks near the shadow are attributed to the stretching vibrations of Cu-O).

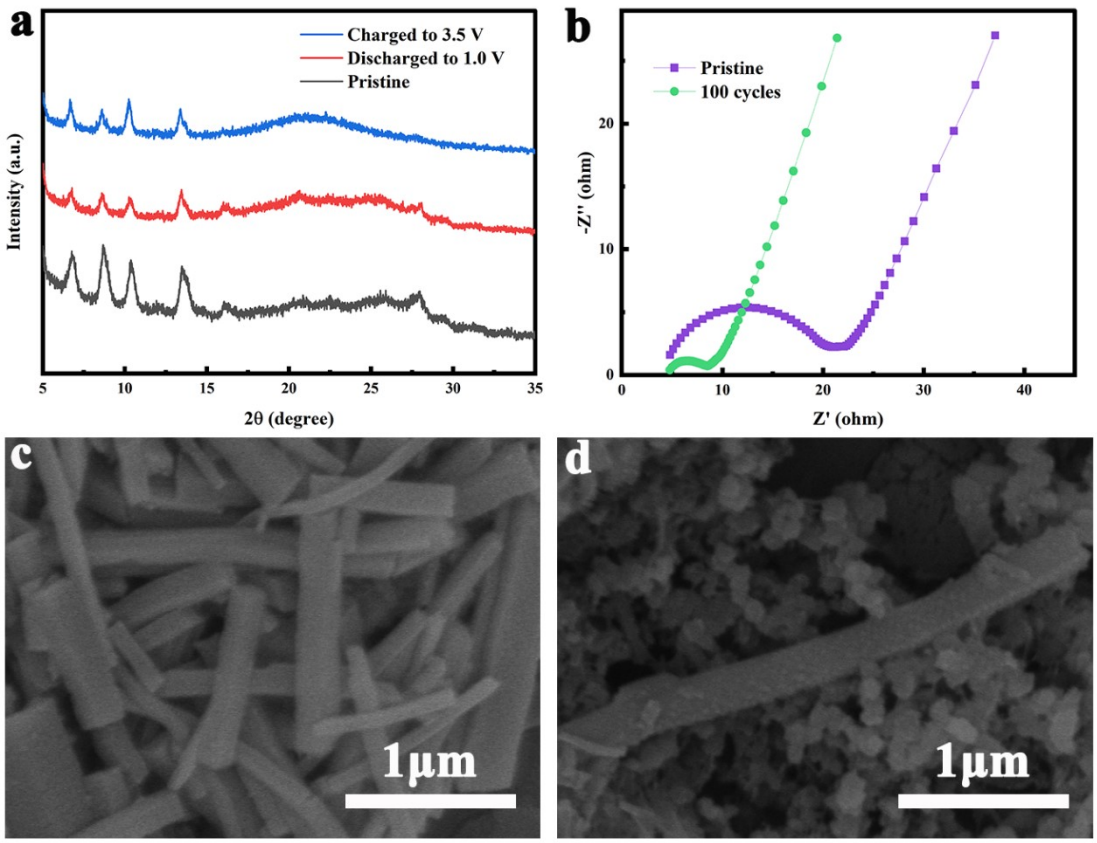

Figure S27. (a) *Ex-situ* PXRD patterns of Cu-DBC cathode during the GCD process. (b) Electrochemical impedance spectra of Cu-DBC cathodes after long cycles. The SEM images of Cu-DBC before (c) and after (d) 100 cycles.

Table S1. EXAFS fitting parameters at the Cu K-edge for Cu-DBC.

Sample	Shell	N	R(Å)	σ^2(Å^2)	E_0	R factor
Cu-DBC	Cu-O	3.37	1.92	0.00132	0.857	0.023
	Cu-O	1.80	2.12	0.00132	0.857	
	Cu···C	2.41	3.27	0.00132	0.857	

N, coordination number; R, the distance to the neighboring atom; σ^2, the Mean Square Relative Displacement (MSRD); E_0, inner potential correction; R factor indicates the goodness of the fit.

Table S2. Comparison of electrochemical performance between the typical cathodes and Cu-DBC cathode for SIBs.

	Capacity [mAh g^{-1}@mA g^{-1}]	Cycle life [cycles, retention%@ A g^{-1}]	Rate performance [mAh g^{-1}@ A g^{-1}]	active material content	Refs.
$Na_3V_{1.5}Cr_{0.5}(PO_4)_3$	163@15	2650, 72@0.75	128@1.5	80%	17
NMTVP	118.5@12	4500,86@0.6	59.3@0.6	70%	18
O3-NNAMO	110@17	200,86@0.085	20@1.7	70%	19
$Na_{2/3}Ni_{1/3}Mn_{2/3}O_2$	89@17.3	1200,71.2@1.73	58.2@3.5	80%	20
MnNi-PB	93.9@15	700,85.3@0.75	69.4@15	70%	21
$Ni_3(HATQ)_2$	108.1@100	1000,95@1	77.1@2	60%	22
Cu-TBA	153.6@50	3000,100@1	50.1@5	40%	23
Co_2(TTFTB)	195@100	200,42@0.1	40@1	30%	24
NiCoFe-PBA	145@15	600,90@0.75	90@1.5	70%	25
UiO-abdc	100@10	150,100@0.01	35@1	60%	26
Cu -DBC	120.6@50	4000,81.9@2	77@5	60%	This work
Cu -DBC	104.4@50	1100,67@1	15.5@5	80%	This work
$Na_2C_6O_6$	190.0@25	100,95@0.025	95.0@0.25	70%	27
PTCDA	145@10	200,80@0.2	91@1	70%	28
PYT-TABQ /rGO	245@200	1400,98@1	141.5@8	60%	29
PTCDI	140@10	300,90@0.2	103@0.6	70%	30
Hollow PPy	97@20	1000,78.5@0.4	87@0.32	80%	31

Section S4. References

[1] J. Liu, Y. Zhou, Z. Xie, Y. Li, Y. Liu, J. Sun, Y. Ma, O. Terasaki, L. Chen, *Angew. Chem.-Int. Edit.*, 2020, **59**, 1081-1086.

[2] Y. Chen, Q. Zhu, K. Fan, Y. Gu, M. Sun, Z. Li, C. Zhang, Y. Wu, Q. Wang, S. Xu, J. Ma, C. Wang, W. Hu, *Angew. Chem.-Int. Edit.*, 2021, **60**, 18769-18776.

[3] M. J. Frisch, G. W. Trucks, H. B. Schlegel, G. E. Scuseria, M. A. Robb, J. R. Cheeseman, G. Scalmani, V. Barone, G. A. Petersson, H. Nakatsuji, X. Li, M. Caricato, A. V. Marenich, J. Bloino, B. G. Janesko, R. Gomperts, B. Mennucci, H. P. Hratchian, J. V. Ortiz, A. F. Izmaylov, J. L. Sonnenberg, Williams, F. Ding, F. Lipparini, F. Egidi, J. Goings, B. Peng, A. Petrone, T. Henderson, D. Ranasinghe, V. G. Zakrzewski, J. Gao, N. Rega, G. Zheng, W. Liang, M. Hada, M. Ehara, K. Toyota, R. Fukuda, J. Hasegawa, M. Ishida, T. Nakajima, Y. Honda, O. Kitao, H. Nakai, T. Vreven, K. Throssell, Jr. J. A. Montgomery, J. E. Peralta, F. Ogliaro, M. J. Bearpark, J. J. Heyd, E. N. Brothers, K. N. Kudin, V. N. Staroverov, T. A. Keith, R. Kobayashi, J. Normand, K. Raghavachari, A. P. Rendell, J. C. Burant, S. S. Iyengar, J. Tomasi, M. Cossi, J. M. Millam, M. Klene, C. Adamo, R. Cammi, J. W. Ochterski, R. L. Martin, K. Morokuma, O. Farkas, J. B. Foresman, D. J. Fox, Gaussian 16 Revision C.01, Gaussian Inc., Wallingford CT, 2016.

[4] C. Lee, W. Yang, R. G. Parr, *Phys. Rev. B*, 1988, **37**, 785-789.

[5] A. D. Becke, *Phys. Rev. A*, 1988, **38**, 3098-3100.

[6] F. Weigend, R. Ahlrichs, *Phys. Chem. Chem. Phys.*, 2005, **7**, 3297-3305.

[7] T. Lu, F. Chen, *J. Comput. Chem.*, 2012, **33**, 580-92.

[8] W. Humphrey, A. Dalke, K. Schulten, *J. Mol. Graphics*, 1996, **14**, 33-38.

[9] G. Kresse, J. Furthmüller, *Comput. Mater. Sci.*, 1996, **6**, 15-50.

[10] G. Kresse, J. Furthmüller, *Phys. Rev. B*, 1996, **54**, 11169-11186.

[11] I.-H. Lee, R. M. Martin, *Phys. Rev. B*, 1997, **56**, 7197-7205.

[12] J. P. Perdew, K. Burke, M. Ernzerhof, *Phys. Rev. Lett.*, 1996, *77*, 3865-3868.

[13] S. Grimme, *J. Comput. Chem.*, 2006, **27**, 1787-1799.

[14] A. I. Liechtenstein, V. I. Anisimov, J. Zaanen, *Phys. Rev. B*, 1995, **52**, R5467-R5470.

[15] L. Wang, T. Maxisch, G. Ceder, *Phys. Rev. B*, 2006, **73**, 195107.

[16] H. J. Monkhorst, J. D. Pack, *Phys. Rev. B*, 1976, **13**, 5188-5192.

[17] M. Chen, W. Hua, J. Xiao, J. Zhang, V. W. Lau, M. Park, G. H. Lee, S. Lee, W. Wang, J. Peng, L. Fang, L. Zhou, C. K. Chang, Y. Yamauchi, S. Chou, Y. M. Kang, *J. Am. Chem. Soc.*, 2021, **143**, 18091-18102.

[18] P. Hu, C. Cai, X. Li, Z. Wei, M. Wang, C. Chen, T. Zhu, L. Mai, L. Zhou, *Adv. Funct. Mater.*, 2024, **34**, 2302045.

[19] B. Peng, Y. Chen, L. Zhao, S. Zeng, G. Wan, F. Wang, X. Zhang, W. Wang, G. Zhang, *Energy Storage Mater.*, 2023, **56**, 631-641.

[20] Q. Liu, Z. Hu, M. Chen, C. Zou, H. Jin, S. Wang, Q. Gu, S. Chou, *J. Mater. Chem. A*, 2019, **7**, 9215-9221.

[21] Z. Xu, Y. Sun, J. Xie, Y. Nie, X. Xu, J. Tu, J. Zhang, L. Qiu, T. Zhu, X. Zhao, *ACS Sustain. Chem. Eng.*, 2022, **10**, 13277-13287.

[22] D. Chen, L. Cheng, W. Chen, H. G. Wang, F. Cui, L. Chen, *Chem. Sci.*, 2024, **15**, 11564-11571.

[23] M. Qi, L. Cheng, H. G. Wang, F. Cui, Q. Yang, L. Chen, *Adv. Mater.*, 2024, **36**, e2401878.

[24] K. Wakamatsu, S. Furuno, Y. Yamaguchi, R. Matsushima, T. Shimizu, N. Tanifuji, H. Yoshikawa, *ACS Appl. Energ. Mater.*, 2023, **6**, 9124-9135.

[25] J. Peng, J. Wang, H. Yi, W. Hu, Y. Yu, J. Yin, Y. Shen, Y. Liu, J. Luo, Y. Xu, P. Wei, Y. Li, Y. Jin, Y. Ding, L. Miao, J. Jiang, J. Han, Y. Huang, *Adv. Energy Mater.*, 2018, **8**, 1702856.

[26] A. V. Desai, V. R. Seymour, R. Ettlinger, A. Pramanik, A. G. Manche, D. N. Rainer, P. S. Wheatley, J. M. Griffin, R. E. Morris, A. R. Armstrong, *Chem. Commun.*, 2023, **59**, 1321–1324.

[27] Y. Wang, Y. Ding, L. Pan, Y. Shi, Z. Yue, Y. Shi, G. Yu, *Nano Lett.*, 2016, **16**, 3329-3334.

[28] W. Luo, M. Allen, V. Raju, X. Ji, *Adv. Energy Mater.*, 2014, **4**, 1400554.

[29] Y. Chen, H. Li, M. Tang, S. Zhuo, Y. Wu, E. Wang, S. Wang, C. Wang, W. Hu, *J. Mater. Chem. A*, 2019, **7**, 20891-20898.

[30] W. Deng, Y. Shen, J. Qian, Y. Cao, H. Yang, *ACS Appl. Mater. Interfaces*, 2015, **7**, 21095-21099.

[31] D. Su, J. Zhang, S. Dou, G. Wang, *Chem. Commun.*, 2015, **51**, 16092-16095.